RSC Advances

PAPER

View Article Online
View Journal | View Issue

Cite this: *RSC Adv.*, 2017, **7**, 16189

Preparation and exceptional adsorption performance of porous MgO derived from a metal–organic framework†

Xian-He Shi, Jin-Jin Ban, Li Zhang, Zhi-Peng Sun, Dian-Zeng Jia* and Guan-Cheng Xu*

Received 13th January 2017
Accepted 5th March 2017

DOI: 10.1039/c7ra00526a

rsc.li/rsc-advances

Porous MgO materials have unique and highly attractive properties. In this paper, porous MgO microstructures with hexagonal and double hexagonal pyramid architectures (MgO-hex and MgO-dhp) were prepared simply by annealing Mg-based metal–organic framework $[NH_4][Mg(HCOO)_3]$. The monodisperse porous MgO-hex and MgO-dhp products inherit the morphologies of the $[NH_4][Mg(HCOO)_3]$ precursors and have large surface areas. The adsorption performance of porous MgO-hex and MgO-dhp were systematically tested towards Congo red (CR) as a model pollutant. The adsorption capacities are 1380 mg g^{-1} for MgO-hex and 1413 mg g^{-1} for MgO-dhp toward CR after 150 minutes at the initial concentration of 1000 mg L^{-1}. The prepared MgO materials exhibit potential applications in wastewater treatment. The experimental data were fitted by two isotherm models, and the adsorption isotherm obeys the Langmuir model. Moreover, the kinetic studies indicate that the kinetic data followed a pseudo-second-order model.

1. Introduction

Metal–organic frameworks (MOFs) are a novel class of inorganic–organic materials with intriguing properties and possible applications as functional materials in gas storage and separation,[1–3] catalysis,[4,5] adsorption,[6,7] air purification[8,9] and so on. With enormous choices of metal ions or metal ion clusters and bridging organic ligands, MOFs have diverse compositions, morphologies and controllable sizes, and thus have attracted global attention.[10–13] Until now, the structures and morphologies of MOFs have been extensively studied.[10–16] For instance, Boom *et al.* obtained different MOF morphologies by changing reaction conditions (*i.e.*, solvent ratio, reaction time, anaerobic/aerobic conditions).[15] Kitagawa's group fabricated different MOF morphologies by increasing the concentration of modulator (*n*-dodecanoic acid/lauric acid) without changing material composition.[16] Furthermore, microscale and nanoscale MOFs with various morphologies have become promising precursors or templates to prepare a new class of highly tailorable porous microstructured and nanostructured materials, such as porous metal oxides, carbon materials and carbon composite materials under different calcination conditions and atmospheres.[17,18] When MOFs are calcined in air at a suitable temperature, the metal ions therein are transformed into metal oxides, and C and other elements (*e.g.* N and H) can be oxidized into gaseous products, and the porous structures are formed at the same time.[19,20] Based on the decomposition of MOF-5 precursor, Wei *et al.* prepared hierarchical ZnO parallelepipeds with the thicknesses of around 300–500 nm, and the morphology of ZnO completely inherited that of MOF-5.[21] Kuang's team synthesized highly porous Co_3O_4 concave nanocubes by simply calcining cobalt-based zeolitic imidazolate framework-67 at an optimized temperature. The nanocubes have good gas-sensing property and the highest sensitivity to ethanol with fast response.[22] However, to the best of our knowledge, MOFs have rarely been used as precursors to prepare MgO materials, especially porous MgO with different shapes.[23] Recently, several methods have been proposed to prepare nanoscale MgO materials.[24–26] Xia *et al.* described a vapor-phase method for the preparation of MgO nanowires from magnesium diboride (MgB_2), involving a series of time-consuming steps.[24] Gedanken and co-workers prepared small MgO nanocrystallines with non-uniform shapes by a microwave-assisted radiation procedure from $Mg(OH)_2$, requiring special equipments and high temperature though.[25] Šubrt *et al.* synthesized MgO nanoparticles with irregular shapes by sonochemical synthesis from $Mg(OCH_3)_2$ and $Mg(OC_2H_5)_2$, but special equipments and expensive alkoxide were needed.[26] Therefore, it is still challenging to develop a simple method for preparation of porous and monodisperse MgO particles with various shapes. As mentioned above, many kinds of porous metal oxides have been prepared by calcining MOFs, so MOFs can also be used as

Key Laboratory of Energy Materials Chemistry, Ministry of Education, Key Laboratory of Advanced Functional Materials, Autonomous Region, Institute of Applied Chemistry, Xinjiang University, Urumqi, 830046 Xinjiang, PR China. E-mail: xuguanchengxju@163.com; jdz@xju.edu.cn

† Electronic supplementary information (ESI) available. See DOI: 10.1039/c7ra00526a

precursors to prepare porous MgO materials. In a previous study, we fabricated a series of metal-formate frameworks. Among them, the Mg-based metal–organic framework $[NH_4][Mg(HCOO)_3]$ crystallizes in the hexagonal chiral space group $P6_322$ with a $(4^9\cdot6^6)$ network topology. The Mg^{2+} ion is coordinated by six formate anions, and formate anion connects two Mg^{2+} ions with the anti–anti bridging mode. NH_4^+ cations are located in the hexagonal channels of the framework.[27] $[NH_4][Mg(HCOO)_3]$ has excellent thermal stability and large amounts of gas can be produced during thermal decomposition. Therefore, $[NH_4][Mg(HCOO)_3]$ can be utilized as ideal precursor for the preparation of porous MgO. On the other hand, water pollution has become a serious environmental problem for the society at present. Especially, non-biodegradable organic dyes exert evident detrimental effects on the environment and human health.[28–30] Recently, a heated discussion was focused on removing of such dyes from the wastewater. Consequently, it is necessary to develop a method with high efficiency and low cost to remove organic dye pollutants. In traditional techniques (coagulation, flocculation, reverse osmosis, and activated carbon adsorption) for treating the dye-containing in wastewater, adsorption is the best method among those techniques due to its simple operation, high treatment efficiency and economy.[31] MgO is a nontoxic, economical and environmentally friendly adsorbent material which can adsorb organic dyes and heavy metal ions. Recently, the applications of porous MgO in water treatment have been reported.[32–34] Ai *et al.* prepared the mesoporous MgO by direct thermal transformation of the sacrificial oxalate template. The maximum adsorption capacity of mesoporous MgO toward Congo red (CR) reaches 689.7 mg g^{-1}.[32] In addition, the nanorod, hierarchical nanostructure and nanoflake MgO were prepared by precipitation, reflux and hydrothermal methods, respectively. The hierarchical MgO nanostructure exhibits the adsorption performance for removal CR with maximum adsorption capacity of 1050.81 mg g^{-1}.[34] Ning and co-workers synthesized the porous hierarchical MgO by a scaled-up method. The maximum adsorption capacity of CR on the hierarchical MgO reached above 2400 mg g^{-1}.[35] Su *et al.* prepared the lamellar MgO by a phase transfer method. The maximum adsorption capacity of lamellar MgO can reach up to 2650 mg g^{-1}.[36] In despite of these achievements at present, the synthesis methods and the adsorption capacities of MgO need to be further improved.

In this study, we successfully synthesized highly monodisperse MOFs $[NH_4][Mg(HCOO)_3]$ with hexagonal and double hexagonal pyramid morphologies by changing the reaction time. Subsequently, a thermal transformation process was introduced to completely convert the $[NH_4][Mg(HCOO)_3]$ precursors into porous MgO products which retain the original morphologies. The adsorption properties of the synthesized MgO products were tested. Both MgO-hex and MgO-dhp showed superb adsorption performance.

2. Experimental

2.1 Materials

All analytical-grade chemicals and solvents were obtained from commercial sources and used without further purification.

2.2 Characterizations

Powder X-ray diffraction (XRD) was performed by a Bruker D8 advance X-ray diffractometer at a scanning rate of 2° min^{-1} in 2θ ranging from 10° to 80° with Cu/Kα radiation (λ = 1.54178 Å). Thermogravimetric analysis (TGA) measurements were carried out on a Netzsch STA 449F3 Model instrument in dynamic N_2 atmosphere with the heating rate of 5 K min^{-1}. Morphology and microstructure of the particles were investigated by Hitachi S-4800 scanning electron microscope (SEM), H-600 transmission electron microscope (TEM) and JEM-2100 HR transmission electron microscope (HRTEM). The sizes of the particles were tested by the nano measurement software. Nitrogen adsorption and desorption isotherms were measured at 77 K with a Micromeritics ASAP 2020 apparatus. Specific surface areas were calculated by the Brunauer–Emmett–Teller (BET) method, and pore diameters were calculated by Barrett–Joyner–Halenda (BJH) method. Ultraviolet-visible (UV-vis) spectra were recorded on a Hitachi U-3900H spectrophotometer.

2.3 Preparation of $[NH_4][Mg(HCOO)_3]$ precursors and MgO products

Metal–organic framework $[NH_4][Mg(HCOO)_3]$ microparticles with hexagonal and double hexagonal pyramid shapes were synthesized through quick mixing of reactants in a methanol solution by changing the reaction time, without the addition of any modulators or surfactants. For the preparation of hexagonal $[NH_4][Mg(HCOO)_3]$ precursor, the reaction was performed with $MgCl_2\cdot6H_2O$, ammonium formate and formic acid at a concentration ratio of 1 : 4 : 2. A methanol solution (20.0 mL) of $MgCl_2\cdot6H_2O$ (0.15 M) was mixed with another methanol solution (20.0 mL) of ammonium formate (0.60 M) and formic acid (0.30 M). The solution was stirred for 5 minutes at room temperature. Colorless stereo hexagonal crystals of $[NH_4][Mg(HCOO)_3]$ were harvested, washed several times with methanol and dried in vacuum at 50 °C for 1 h. Hexagonal $[NH_4][Mg(HCOO)_3]$ was referred to as Mg-MOF-hex, according to the abbreviation of metal–organic framework and the first three letters of morphology name. When the stirring time was extended to 40 minutes, double hexagonal pyramid particles of $[NH_4][Mg(HCOO)_3]$ were obtained and referred to as Mg-MOF-dhp. Other conditions remained unchanged.

For the preparation of porous MgO products, Mg-MOF-hex and Mg-MOF-dhp particles were calcined at 450 °C for 2 h with a ramping rate of 5 °C min^{-1} in nitrogen atmosphere; yield white MgO-hex and MgO-dhp products, respectively.

2.4 Evaluation of adsorption performance

CR ($C_{32}H_{22}N_6Na_2O_6S_2$), an azo anionic dye, has been used as a model pollutant for dye removal.[14] CR adsorption was tested in duplicate by shaking at the speed of 150 rpm using 25 mL conical flasks. To study kinetic, 0.01 g of the MgO-hex and MgO-dhp samples were mixed with 15 mL of CR solution (100 mg L^{-1}, 300 mg L^{-1}, 700 mg L^{-1}, 1000 mg L^{-1}) for different time periods, respectively. The adsorption isotherms were finished by mixing MgO (0.01 g) to CR solutions (15 mL) of different

initial concentrations for 150 minutes at room temperature. The concentration of CR left in the supernatant was tested by using a Hitachi U-3900H spectrophotometer. The adsorption capacities of CR on MgO-hex and MgO-dhp were calculated by:

$$q_e = \frac{V(C_0 - C_e)}{m} \quad (1)$$

where q_e is the adsorption capacity (mg g^{-1}), C_0 and C_e are the concentrations of CR (mg L^{-1}) before and after adsorption, respectively, m is the mass of MgO sample (g) and V is the volume of solution (L).

The effects of MgO-hex and MgO-dhp dosages were assessed by mixing different weights of MgO-hex and MgO-dhp samples with 15 mL of 250 mg L^{-1} CR solution for 30 minutes, respectively. The weights of MgO-hex and MgO-dhp were adjusted from 0.06 to 0.5 g L^{-1}. The following experiments were carried out to study the behavior of MgO-hex and MgO-dhp adsorption for different time periods. In a typical process, a 15 mL mixture contained CR at an initial concentration of 250 mg L^{-1} and 0.01 g MgO-hex or MgO-dhp, the two components were thoroughly mixed in a flask at room temperature for 30 minutes. MgO samples were separated from the mixture by centrifugation after adsorption, and the concentration of CR left in the supernatant was tested by using the spectrophotometer. More information on the calculation of the CR concentration by UV-vis has been given in the ESI† (Experimental section).

3. Results and discussion

3.1 Characterizations of $[NH_4][Mg(HCOO)_3]$ precursors

The XRD patterns of Mg-MOF-hex and Mg-MOF-dhp precursors and the simulation result of single crystal $[NH_4][Mg(HCOO)_3]$ are presented in Fig. 1. All the diffraction peaks of Mg-MOF-hex and Mg-MOF-dhp are in good agreement with that of the simulated pattern,[27] indicating that the obtained precursors are pure and highly crystalline.

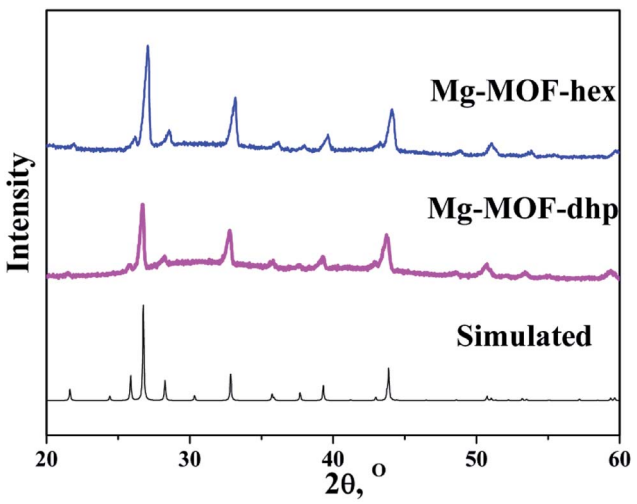

Fig. 1 Simulated XRD pattern derived from crystallographic data and XRD patterns of Mg-MOF-hex and Mg-MOF-dhp.

The morphology and size of Mg-MOFs were characterized by SEM. Two different morphologies of Mg-MOFs were obtained by changing the reaction time. They are uniform and monodisperse particles with hexagonal (Fig. 2a) and double hexagonal pyramid morphologies (Fig. 2c). As exhibited in the high-magnification SEM images (Fig. 2b and d), the average sizes of Mg-MOF-hex and Mg-MOF-dhp are about 3.85 μm and 3.22 μm, respectively. The particle sizes and distributions of the Mg-MOFs are shown in Fig. S2,† we found that the Mg-MOF-dhp particles are more uniform than the Mg-MOF-hex particles. The hexagonal and double hexagonal pyramid structures both present well-defined flat and smooth exterior surfaces. Therefore, the reaction time has a pronounced effect on the growth and morphology of the final products.[37]

The TGA results of Mg-MOF-hex and Mg-MOF-dhp are shown in Fig. S1.† Their thermal decomposition takes place in two distinguishable stages. The first weight losses in the temperature range of 130–240 °C are 37.21% and 36.44%, respectively,

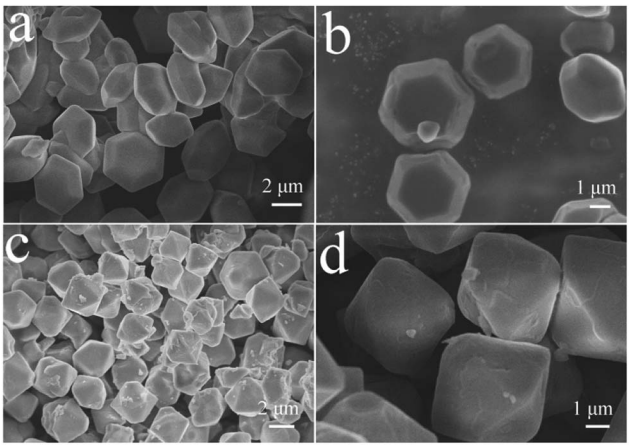

Fig. 2 SEM images of Mg-MOF-hex (a and b) and Mg-MOF-dhp (c and d).

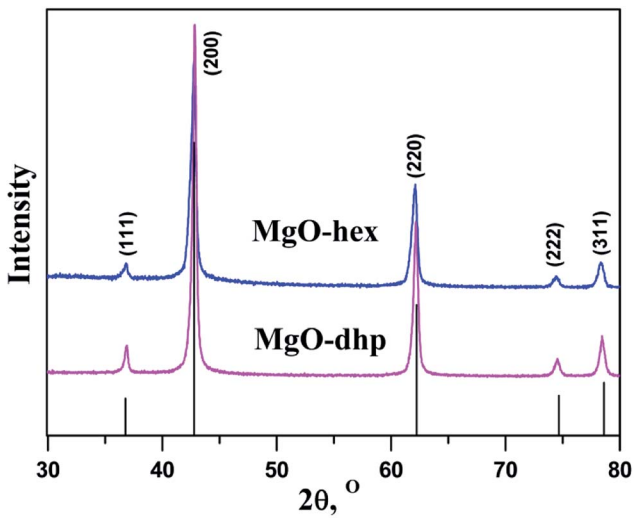

Fig. 3 Powder XRD patterns of MgO-hex and MgO-dhp.

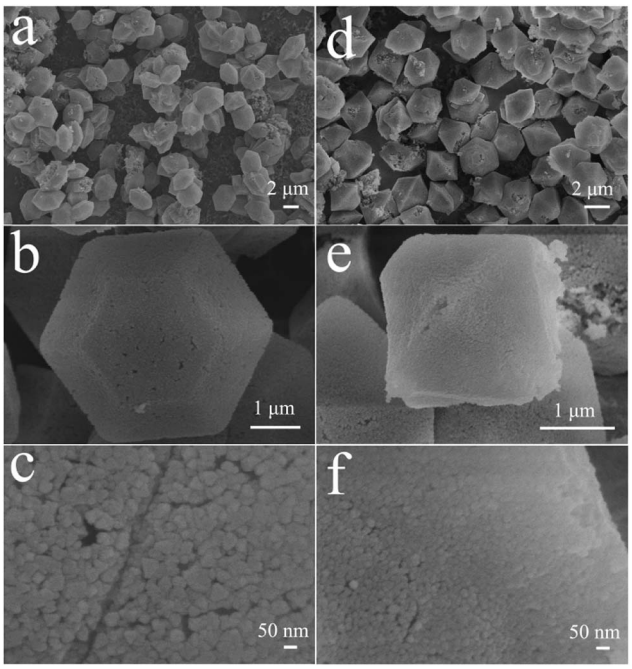

Fig. 4 SEM images of MgO-hex (a–c) and MgO-dhp (d–f).

corresponding to the loss of one ammonium cation and one formate anion per formula. The observed mass losses are in good agreement with the calculated value (calcd 35.54%). Afterwards, the second stage occurs in the temperature range of 300–450 °C, corresponding to the decomposition of residual formate ligands. The observed mass losses (41.22% and 41.95%) are also consistent with the theoretical value (41.74%). The final residues of Mg-MOF-hex and Mg-MOF-dhp are 21.57% and 21.61% respectively, being in accordance with the calculated value (22.72%) based on MgO. The TGA results suggest that MgO products can be obtained by calcination at 450 °C.

3.2 Characterizations of the MgO particles

Mg-MOF-hex and Mg-MOF-dhp were used as the precursors to synthesize MgO by a thermal decomposition process. Based on TGA results, calcinations were performed at 450 °C for 2 h at a ramping rate of 5 °C min^{-1} in nitrogen atmosphere to complete the conversion. The structure and phase purity of MgO products were examined by XRD (Fig. 3). All the diffraction peaks of MgO-hex and MgO-dhp products can clearly be indexed to MgO (JCPDS No. 45-0946). Since there are no additional diffraction peaks from residues or impurities, the Mg-MOF precursors have been completely transformed into MgO with high purity.

The MgO-hex and MgO-dhp microparticles with distinct morphologies and structures are displayed in Fig. 4. In low-magnification SEM images (Fig. 4a and d), the microparticles are monodisperse and uniform. In high-magnification SEM images (Fig. 4b and e), the microparticles retain the size and shapes of Mg-MOFs precursors well. Besides, the surfaces of MgO-hex and MgO-dhp products are very rough and decorated with many pores, indicating the formation of pores during calcination. From Fig. 4c and f, we can see that the MgO-hex and MgO-dhp microparticles are composed of small MgO nanoparticles. The obtained MgO materials are further characterized by TEM. As shown in Fig. 5, the hexagonal (Fig. 5a and b) and double hexagonal pyramid (Fig. 5d and e) MgO materials have well-defined morphologies and porous structures, which are composed of small nanoparticles. As shown in the HRTEM images (inset in Fig. 5b and e), the sizes of these nanoparticles

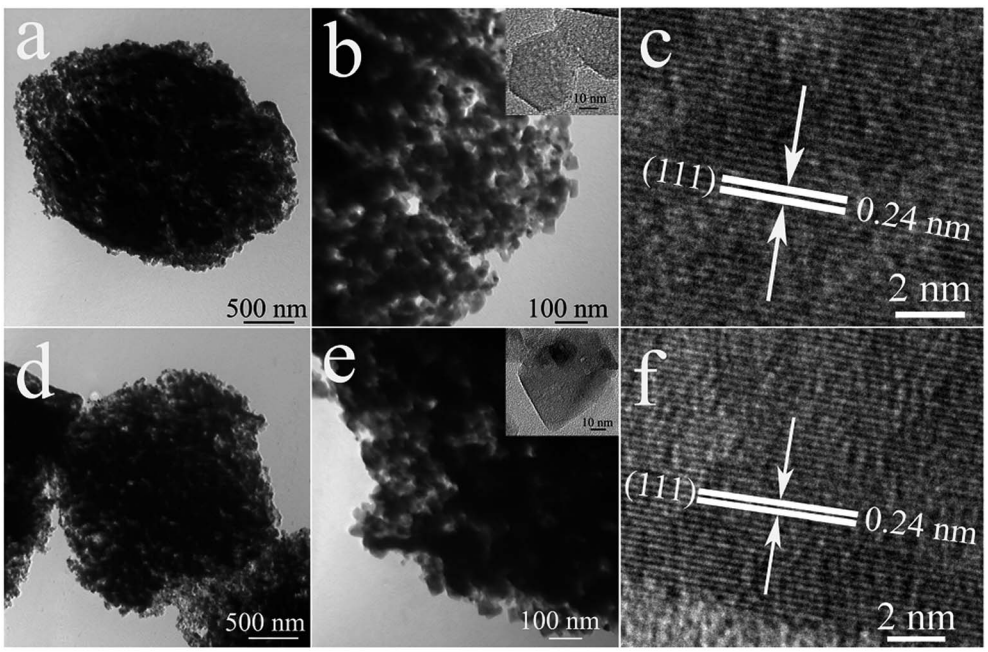

Fig. 5 TEM images of MgO-hex (a and b) and MgO-dhp (d and e). HRTEM images of MgO-hex (inset in b and c) and MgO-dhp (inset in e and f).

are about 50 nm and 30 nm, respectively. And HRTEM images (Fig. 5c and f) show that the *d*-spacing value is approximately 0.24 nm, corresponding to the (111) plane of MgO-hex and MgO-dhp, respectively.

To further analyze the porous structures of MgO-hex and MgO-dhp architectures, nitrogen adsorption–desorption measurements were carried out (Fig. 6). The adsorption–desorption isotherms of MgO-hex and MgO-dhp both present type IV hysteresis loops at high relative pressures (P_e/P_0) (0.8–1.0), which confirm their mesoporous structures. The mesopores were generated by the aforementioned gas release during calcination. The BET surface areas of MgO-hex and MgO-dhp are 92 $m^2\ g^{-1}$ and 102 $m^2\ g^{-1}$, respectively. The pore sizes exhibit unimodal distributions (insets in Fig. 6a and b), and the mesopores in MgO-hex and MgO-dhp have the peak diameters of 3–6 nm and 2–5 nm, respectively, *i.e.* they both have porous structures.

Given that the as-prepared porous MgO-hex and MgO-dhp architectures have large specific areas and porous structures, they may be applied to the adsorption of organic pollutants in water. Their adsorption performances were tested by using CR as the organic dye. Fig. 7a and b show the time profiles of CR adsorption at different initial concentrations with 0.01 g MgO-hex and MgO-dhp in 15 mL CR solution for 150 minutes. The adsorptions are very fast in the first 10 minutes at all concentrations. Furthermore, the adsorption rate of MgO-dhp surpasses that of MgO-hex. The adsorptions are almost finished in about 30 minutes, indicating that CR in water is rapidly adsorbed by MgO-hex and MgO-dhp. Notably, MgO-hex and MgO-dhp exhibit super-high adsorption capacities (1380 and 1413 mg g^{-1}, respectively) toward CR after 150 minutes at the initial concentration of 1000 mg L^{-1}. The particle sizes and BET surface areas are 3.85 (3.22) μm and 92 (102) $m^2\ g^{-1}$ for MgO-hex (MgO-dhp), respectively. These results indicate that the specific surface areas increase with decreasing the particle sizes. The powerful abilities of CR removal for the porous MgO materials are mainly attributed to their advantageous structure (*e.g.* small size, high specific surface area and porous structure). Thus the adsorption capacity of MgO-dhp is higher than that of MgO-hex. To further examine the adsorption capacities, as shown in Fig. 7c and d, we recorded the UV-vis absorption spectra of CR solutions before and after being treated by different dosages of MgO-hex (Fig. 7c) and MgO-dhp (Fig. 7d) with a fixed initial CR concentration of 250 mg L^{-1}. The removal efficiency of CR increases with rising MgO dosage. Particularly, at a dosage of 0.5 g L^{-1}, CR is almost completely absorbed. Fig. S3† shows the UV-vis absorption spectra of CR solutions (250 mg L^{-1}) before and after being treated by MgO-hex and MgO-dhp for different time periods. The absorption efficiency of MgO-dhp is much higher than that of MgO-hex.

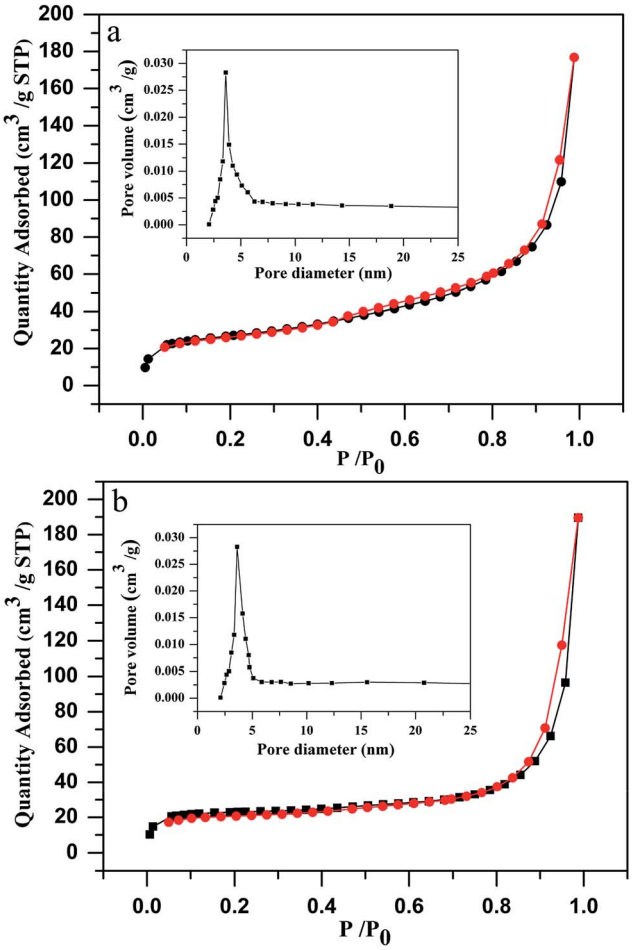

Fig. 6 Nitrogen adsorption–desorption isotherms of MgO-hex (a) and MgO-dhp (b). Inset shows the corresponding BJH pore size distribution.

The Langmuir (eqn (2)) and Freundlich isotherm models (eqn (3)) were used to describe these adsorption processes,[26]

$$\ln q_e = \frac{1}{n}\ln C_e + \ln k_f \quad (2)$$

$$\frac{C_e}{q_e} = \frac{1}{k_L q_m} + \frac{C_e}{q_m} \quad (3)$$

where C_e (mg L^{-1}) is the equilibrium concentration of CR after treatment with MgO samples, and q_e (mg g^{-1}) is the adsorption capacity at equilibrium. K_L (L mg^{-1}) and q_m (mg g^{-1}) are the Langmuir constants related to affinity parameter and the maximum adsorption capacity. K_f (L g^{-1}) and n are the Freundlich constants, representing the adsorption capacity and the heterogeneity factor, respectively. The Langmuir and Freundlich isotherm constants are shown in Fig. S4 and S5.† The kinetic parameters are given in Tables S1 and S2.† Clearly, the adsorption data of both MgO-hex and MgO-dhp are fitted better by the Langmuir model ($R^2 = 0.992$ and 0.993) than by the Freundlich model (R^2 = 0.953 and 0.955), indicating the adsorption follows a monolayer mechanism.

The kinetics of CR removal by MgO-hex and MgO-dhp were further investigated. The pseudo-first-order and pseudo-second-order kinetic models were applied to describe the adsorption processes,[26]

$$\log(q_e - q_t) = \log q_e - \frac{k_1 t}{2.303} \quad (4)$$

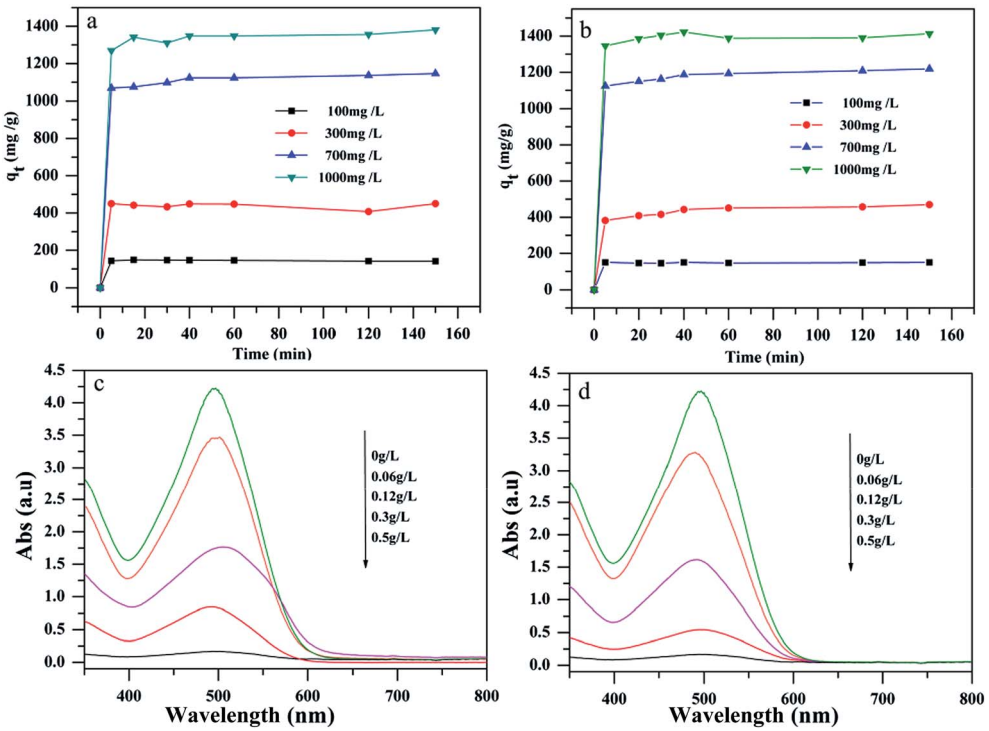

Fig. 7 Time profiles of CR adsorption on MgO-hex (a) and MgO-dhp (b). UV-vis absorption spectra of CR solutions before and after being treated by different dosages of MgO-hex (c) and MgO-dhp (d).

$$\frac{t}{q_t} = \frac{1}{k_2 q_e^2} + \frac{t}{q_e} \quad (5)$$

where q_e and q_t (g mg^{-1} mg g^{-1}) are the adsorption capacities at equilibrium and at any time t (min), respectively. k_1 (g mg^{-1} min^{-1}) and k_2 (g mg^{-1} min^{-1}) are the pseudo-first-order and pseudo-second-order rate constants, respectively.

The kinetic parameters are given in Tables S3 and S4,† and the curve-fitting results are shown in Fig. S6 and S7.† Similarly, the adsorption data are also well fitted by the pseudo-first-order model (Fig. S6†). However, the values of q_e are smaller than those of q_t, indicating that such model is unsuitable to describe the adsorption process. In contrast, the adsorption kinetic data can be fitted by the linear form of the pseudo-second-order model (Fig. S7†). The values of $q_{e,cal}$ are close to those of $q_{e,exp}$, suggesting that the adsorption process of CR on MgO-hex and MgO-dhp follows the pseudo-second-order model. Meanwhile, the high correlation coefficients ($R^2 > 0.999$) also demonstrate that the pseudo-second-order model fits the adsorption kinetics more accurately than the pseudo-first-order one.

4. Conclusions

In summary, Mg-MOF-hex and Mg-MOF-dhp were readily obtained through direct assembly of reactants for different reaction times in methanol. Porous MgO-hex and MgO-dhp materials were obtained by calcinating the Mg-MOFs precursors. The two MgO products were potently remove organic dye CR from water owing to their large surface areas and porous structures. The adsorption capacities are 1380 mg g^{-1} for MgO-hex and 1413 mg g^{-1} for MgO-dhp toward CR after 150 minutes at the initial concentration of 1000 mg L^{-1}. In addition, the adsorption processes of the CR on porous MgO-hex and MgO-dhp were also systematically investigated. It is found that the adsorption processes are fitted well by the Langmuir adsorption model and pseudo-second-orders rate equation. The porous hexagonal and double hexagonal pyramid MgO are expected to be a promising candidate for application due to its simple and cost-effective preparation processes, and excellent dye adsorption capacities.

Acknowledgements

This work was financially supported by National Natural Science Foundation of China (No. 21471127, 21361025, 21661029, 21663029), Natural Science Fund for Distinguished Young Scholars of Xinjiang Uygur Autonomous Region (No. 2013711008). We thank Dr Yuan-Hua Xiao for the HRTEM measurements.

References

1 K. Sumida, D. L. Rogow, J. A. Mason, T. M. McDonald, E. D. Bloch, Z. R. Herm, T. H. Bae and J. R. Long, *Chem. Rev.*, 2012, **112**, 724–781.
2 R. B. Getman, Y. S. Bae, C. E. Wilmer and R. Q. Snurr, *Chem. Rev.*, 2012, **112**, 703–723.
3 H. H. Wu, Q. H. Gong, D. H. Olson and J. Li, *Chem. Rev.*, 2012, **112**, 836–868.

4 C. Pagiś, M. Ferbinteanu, G. Rothenberg and S. Tanase, *ACS Catal.*, 2016, **6**, 6063–6072.
5 Y. Zhang and J. Y. Ying, *ACS Catal.*, 2015, **5**, 2681–2691.
6 N. C. Burtch, H. Jasuja and K. S. Walton, *Chem. Rev.*, 2014, **114**, 10575–10612.
7 M. F. D. Lange, K. J. F. M. Verouden, T. J. H. Vlugt, J. Gascon and F. Kapteijn, *Chem. Rev.*, 2015, **115**, 12205–12250.
8 J. B. DeCoste and G. W. Peterson, *Chem. Rev.*, 2014, **114**, 5695–5727.
9 Y. Y. Zhang, S. Yuan, X. Feng, H. W. Li, J. W. Zhou and B. Wang, *J. Am. Chem. Soc.*, 2016, **138**, 5785–5788.
10 L. N. Jin, Q. Liu and W. Y. Sun, *CrystEngComm*, 2013, **15**, 4779–4784.
11 X. P. Shen, Q. Liu, Z. Y. Ji, G. X. Zhu, H. Zhu and K. M. Chen, *CrystEngComm*, 2015, **17**, 5522–5529.
12 M. Sindoro, N. Yanai, A. Y. Jee and S. Granick, *Acc. Chem. Res.*, 2014, **47**, 459–469.
13 J. Sun, K. L. Wu, X. Z. Li, C. Dong, X. W. Wei, X. W. Wang, B. Zhang, Z. X. Zhang and J. R. Huang, *CrystEngComm*, 2014, **16**, 6873–6881.
14 A. Schoedel, M. Li, D. Li, M. O'Keeffe and O. M. Yaghi, *Chem. Rev.*, 2016, **116**, 12466–12535.
15 S. Shankar, R. Balgley, M. Lahav, S. R. Cohen, R. P. Biro and M. E. Boom, *J. Am. Chem. Soc.*, 2015, **137**, 226–231.
16 A. Umemura, S. Diring, S. Furukawa, H. Uehara, T. Tsuruoka and S. Kitagawa, *J. Am. Chem. Soc.*, 2011, **133**, 15506–15513.
17 H. Y. Shi, B. Deng, S. L. Zhong, L. Wang and A. W. Xu, *J. Mater. Chem.*, 2011, **21**, 12309–12315.
18 Y. Kimitsuka, E. Hosono, S. Ueno, H. Zhou and S. Fujihara, *Inorg. Chem. Commun.*, 2013, **52**, 14028–14033.
19 L. Hua and Q. W. Chen, *Nanoscale*, 2014, **6**, 1236–1257.
20 K. Liu, H. Liu, L. L. Yang, F. Y. Zhao, Y. Li and W. J. Ruan, *RSC Adv.*, 2014, **4**, 25160–25164.
21 Y. F Li, Z. Z. Che, X. Sun, J. Dou and M. D. Wei, *Chem. Commun.*, 2014, **50**, 9769–9772.
22 Y. Y. Lü, W. W. Zhan, Y. He, Y. T. Wang, X. J. Kong, Q. Kuang, Z. X. Xie and L. S. Zheng, *ACS Appl. Mater. Interfaces*, 2014, **6**, 4186–4195.
23 B. Huang, H. Kobayashi and H. Kitagawa, *Chem. Lett.*, 2014, **43**, 1459–1460.
24 Y. Yin, G. Zhang and Y. Xia, *Adv. Funct. Mater.*, 2002, **12**, 293–296.
25 S. Makhluf, R. Dror, Y. Nitzan, Y. Abramovich and A. Gedanken, *Adv. Funct. Mater.*, 2005, **15**, 1708–1715.
26 V. Štengl, S. Bakardjieva, M. Mařìková, P. Bezdička and J. Šubrt, *Mater. Lett.*, 2003, **57**, 3998–4003.
27 G. C. Xu, X. M. Ma, L. Zhang, Z. M. Wang and S. Gao, *J. Am. Chem. Soc.*, 2010, **132**, 9588–9590.
28 J. S. Wu, J. S. Wang, H. Y. Li, Y. C. Du, K. L. Huang and B. X. Liu, *J. Mater. Chem. A*, 2013, **1**, 9837–9847.
29 R. Mallampati, X. J. Li, A. Adin and S. Valiyaveettil, *ACS Sustainable Chem. Eng.*, 2015, **3**, 1117–1124.
30 J. Zhang, B. Yan, H. Ping, Z. Y. Fu, Y. Li, W. M. Wang, H. Wang, Y. C. Wang, J. Y. Zhang and F. Zhang, *RSC Adv.*, 2016, **6**, 472–480.
31 E. N. Seyahmazegi, R. M. Rezaei and H. Razmi, *Chem. Eng. Res. Des.*, 2016, **109**, 824–834.
32 L. H. Ai, H. T. Yue and J. Jiang, *Nanoscale*, 2012, **4**, 5401–5408.
33 C. Y. Cao, J. Qu, F. Wei, H. Liu and W. G. Song, *ACS Appl. Mater. Interfaces*, 2012, **4**, 4283–4287.
34 J. P. Dhal, M. Sethi, B. G. Mishra and G. Hota, *Mater. Lett.*, 2015, **141**, 267–271.
35 P. Tian, X. Y. Han, G. L. Ning, H. X. Fang, J. W. Ye and W. T. Gong, *ACS Appl. Mater. Interfaces*, 2013, **5**, 12411–12418.
36 X. M. Liu, C. Niu, X. P. Zhen, J. Wang and X. T. Su, *J. Mater. Res.*, 2015, **30**, 1639–1647.
37 X. P. Shen, Q. Liu, Z. Y. Ji, G. X. Zhu, H. Zhou and K. M. Chen, *CrystEngComm*, 2015, **17**, 5522–5529.